



# Assessment and Prediction of Rockburst Risk Zones Under Different Structural Plane Shapes

Shunchuan Wu · Shun Han · Yongbing Wang · Zhigen Zhu · Long Chen · Yangyang Nian

Received: 24 October 2022 / Accepted: 5 June 2023 / Published online: 14 June 2023  
© The Author(s), under exclusive licence to Springer Nature Switzerland AG 2023

**Abstract** Many practical engineering experiments show that the structural plane effect plays an important role in the rockburst development process. The mechanical response of the surrounding rock and the distribution and evolution law of rockburst risk zones during the excavation of tunnels with different structural plane shapes were investigated in the article. Based on FLAC<sup>3D</sup> numerical program and introducing the numerical analysis index, we analyzed the distribution of the stress field and displacement field after the tunnel excavation containing different structural plane shapes. Furthermore, we visualized the distribution of risk zone by using the Fish function for secondary programming to study the distribution of rockburst risk zones and its evolution process. The results are drawn as follows: When the tunnel contains the unexposed structural plane, the development

process of the rockburst is concealed and lagged compared to the exposed structural plane. However, the rockburst risk zone will be expanded once the unexposed structural plane is activated. The exposed part of the exposed structural plane releases much energy and has a strong rockburst impact tendency. The vertical structural plane in the sidewall will make the rockburst risk zone expand in the direction of the structural plane and eventually form the rockburst risk zone, similar to a pan between the structural plane and the excavation boundary. The research results can provide a reference for excavation design and construction of similar underground engineering.

**Keywords** Tunnel engineering · Mechanical response · Rockburst risk zones · Structural plane effect · Failure approaching index · Local energy release rate

---

S. Wu · S. Han (✉) · L. Chen · Y. Nian  
School of Civil and Resource Engineering, University of Science and Technology Beijing, Beijing 100083, China  
e-mail: m202110080@xs.ustb.edu.cn

S. Wu  
Faculty of Land Resource Engineering, Kunming University of Science and Technology, Kunming 650093, China

Y. Wang  
Yunnan Chihong Zinc and Germanium Co., Ltd., Qujing 655011, Yunnan, China

Z. Zhu  
CINF Engineering Co., Ltd., Changsha 410019, China

## 1 Introduction

Rockburst is an extremely destructive and sudden geological hazard in the deep hard and brittle rock under high-stress conditions (Adoko et al. 2013; Dai et al. 2021; Feng et al. 2019a). In deep engineering, the dynamic hazards are closely related to its surrounding complex geological structures (e.g. faults, joints, fractures and structural planes, etc.) (Snelling et al. 2013; Wang et al. 2021b; Feng et al. 2019c, 2012; Liu et al. 2019; Zhang et al. 2012). The

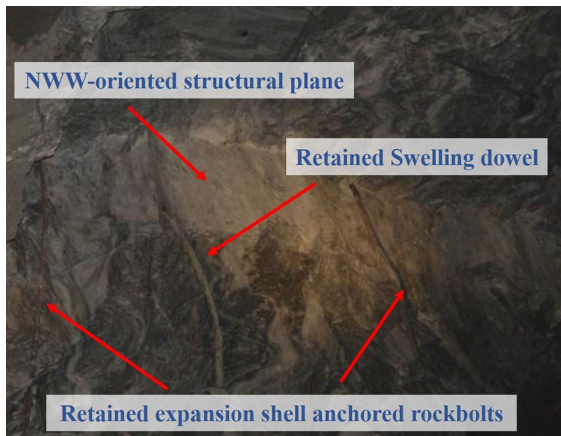


**Fig. 1** Structural plane and retained bolts exposed after “2–4” extremely intense rockburst (Zhang et al. 2012)

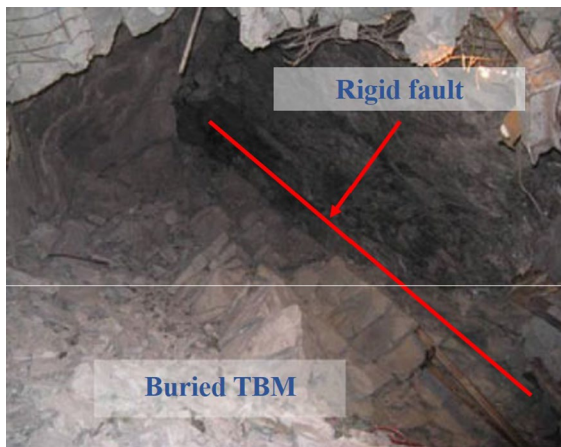


**Fig. 2** Failure zone and exposed structural plane after “11–28” extremely intense rockburst (Zhang et al. 2012)

structural plane is more vulnerable to rockburst, and structural plane-induced rockburst tend to be larger and more destructive, resulting in threats to the lives of workers, damage to construction equipment and huge economic losses, as shown in Figs. 1 and 2. Therefore, the study of structure-type rockburst (structural plane-induced rockburst) is of great engineering significance.

Currently, numerous scholars have conducted a lot of research on the mechanism of rockburst induced by the structural plane. Zhou et al. (2015a) summarised and analyzed the mechanism of the structural plane effect on rockburst under different conditions

and gave a classification method for the structure-type rockburst. Zhou et al. (2015b) revealed three failure mechanisms of structural planes under shear stress based on model experiments using cement mortar and used them to explain the evolution processes of fault slip and shear rupture rockburst. Wu et al. (2022) investigated the rockburst mechanism of rock mass with structural planes during the excavation of the underground chamber based on the model test and numerical simulation. Manouchehrian and Cai (2018) explored the mechanism of rockburst near fault zones in circular tunnels employing Abaqus software. Feng et al. (2019b) used the FDEM approach to study the rupture evolution of deep circular tunnels under the effect of the structural plane during the excavation unloading process, revealing the integrated response mechanism of the structural plane effect and excavation unloading effect. Zhang et al. (2021) investigated the evolution mechanism of the structure-type rockburst based on the particle flow code. Furthermore, the location, dip and thickness of the structural plane, as well as the distance from the structural plane to the tunnel, are proven to be important factors influencing tunnel stability (Huang et al. 2013).

In conclusion, scholars have done a great deal of research on the mechanisms of the structural plane effect. Meanwhile, rockburst assessment and prediction are also important scientific issues in the direction of rockburst research. In the past few decades, rockburst has been estimated using empirical criteria, in-situ monitoring, numerical simulations and mathematical statistics (Zhou et al 2016, 2018; Zhang et al 2017; Liang and Zhao 2022; Askaripour et al. 2022). However, the assessment and prediction of rockburst based on empirical criteria and mathematical statistics do not take into account the influence of the existence of structural planes, and they are primarily employed in the assessment and prediction of strainbursts (Askaripour et al. 2022). In-situ monitoring and numerical simulations are used for the assessment and prediction of structure-type rockburst. Meng et al. (2016) proposed a method to predict fault slip bursts based on b-values in acoustic emission. Liu et al. (2019) obtained rockburst precursor characteristics distributed along the structural plane by analyzing and studying 492 microseismic events recorded in the tunnel of the Hanwei diversion project, which effectively predicted rockburst along the structural plane. Xue et al. (2021) carried out rockburst prediction and

analysis of activity characteristics within surrounding rock based on microseismic monitoring and RFPA<sup>3D</sup>, providing a new idea for strain-structure rockburst prediction.

However, using monitoring techniques for rockburst prediction is costly and vulnerable to environmental and other factors. The rapid development of numerical simulation techniques can compensate for the drawbacks of monitoring techniques. The era of quantitative rockburst prediction has arrived, and many scholars have assessed rockburst risk zones by introducing numerical analysis indexes in numerical simulations (Weng et al. 2017; Wang et al. 2021a; Liang et al. 2022; Zhu et al. 2022; Yang 2015). Among them, the failure approaching index (*FAI*) can quantitatively evaluate the failure zone and damage degree of the rock mass in various regions of engineering and can predict the influence of future excavation disturbance on the stability of the rock mass. Zhang et al. first proposed the concept of *FAI* and evaluated the stability of the underground powerhouse, access tunnels and headrace tunnels of the Jinping II hydropower station by *FAI* (Zhang et al. 2011). Meanwhile, the evolution of the “11–28” structure-type rockburst at Jinping II hydropower station was reproduced by *FAI* (Zhang et al. 2013). Many scholars have applied the *FAI* to the quantitative assessment of the stability of tunnel and slope engineering (Zhang et al. 2007).

At present, the simulation of the excavation process for tunnels containing structural planes is established on a two-dimensional level (Feng et al. 2019b; Feng et al. 2021; Zhang et al. 2021), while the actual excavation process is a three-dimensional continuous dynamic process. In addition, different structural plane shapes may be encountered during the actual excavation process. However, few studies have been reported on assessing and predicting rockburst risk zones in tunnels with different structural plane shapes. Therefore, this study focused on the excavation process of hard rock tunnels with different structural plane shapes. Based on FLAC<sup>3D</sup> software, four working conditions were established: no structural plane, the exposed inclined structural plane, the unexposed inclined structural plane and the vertical structural plane in the sidewall. The failure approaching index (*FAI*) was used to assess and predict rockburst

risk zones. Meanwhile, the local energy release rate (*LERR*) was used to estimate the degree of energy release from the surrounding rock mass, according to which the rockburst intensity can be assessed in the local area (Su et al. 2006). The research results have important engineering significance for designing and constructing similar underground projects.

## 2 Numerical Index Analysis Methods

During the brittle fracture of hard and brittle rock, its cohesion is weakened, but the frictional strength of the crack plane is gradually strengthened. This mechanical mechanism can be described by the hard rock constitutive model of Cohesion Weakening and Frictional Strengthening (*CWFS*) (Hajiabdolmajid and Kaiser 2003). Research has shown that the *CWFS* model for simulating brittle fracture in the hard rock under high-stress conditions is effective and has promising engineering applications (Su and Feng 2005). In the paper, *CWFS* was chosen as the constitutive model for the numerical calculation of surrounding rock, and both *FAI* and *LERR* were introduced to quantitatively analyze and investigate the rockburst development process, and the two numerical indexes are described below.

*FAI* can be quantitatively evaluated by the damage degree of the surrounding rock. It is used to evaluate the risk zone distribution of the surrounding rock and predict the evolution of the risk zone distribution during the excavation process. *FAI* formula is shown in Eq. (1).

$$FAI = \begin{cases} \omega & 0 \leq \omega < 1 \\ \omega + FD & \omega = 1, FD \geq 0 \end{cases} \quad (1)$$

$$\omega = 1 - YAI$$

$$FD = \varepsilon^p / \varepsilon^{pr}$$

where  $\omega$  is the stress risk factor, which is a parameter related to the yield approach index (*YAI*); *FD* (Failure Degree) is an index to evaluate the degree of accumulated damage in the process of deformation and rupture of the rock mass;  $\varepsilon^p$  is the plastic shear strain;  $\varepsilon^{pr}$  is the plastic shear strain limit; *YAI* is the yield approach function considering shear and tension, and the formula is shown in Eq. (2) (Zhou et al. 2005).

$$YAI = \begin{cases} \frac{I_1 \sin \varphi / 3 + (\cos \theta_\sigma - \sin \theta \sin \varphi / \sqrt{3}) \sqrt{J_2} - c \cos \varphi}{I_1 \sin \varphi / 3 - c \cos \varphi} & \frac{\sigma_1 + \sigma_3}{2} \leq \sigma_R \\ \frac{\sigma_t - \sigma_1}{\sigma_t - \sigma_R} & \frac{\sigma_1 + \sigma_3}{2} > \sigma_R \end{cases} \quad (2)$$

where  $c$  and  $\varphi$  are the cohesion and internal friction angle, respectively;  $\sigma_t$  is the tensile strength;  $I_1$  is the first invariant of the stress tensor;  $J_2$  is the second invariant of the partial stress tensor;  $\theta_\sigma$  is the stress Lodder angle;  $\sigma_R$  is the normal stress at point P in Fig. 3, and the formula is shown in Eq. (3).

$$\sigma_R = \frac{\sigma_t(2 - \sin \varphi) - 2c \cos \varphi}{2(1 - \sin \varphi)} \quad (3)$$

The excavation disturbance process of underground rock engineering will break the balance of the initial geo-stress field and form a secondary stress field. Based on the degree of damage to the surrounding rock (failure approaching index), the rock mass around the underground excavation engineering is divided into failure zone ( $FAI \geq 2.0$ ), damage zone ( $1.0 \leq FAI < 2.0$ ), disturbed zone ( $0.8 \leq FAI < 1.0$ ) and in-situ stress zone ( $0.0 \leq FAI < 0.8$ ), where the failure zone (rockburst risk zone) is considered to be the area most prone to rockburst. Meanwhile, the minimum threshold of the excavation disturbed zone is set to 0.8 in this paper (Zhang et al. 2007). The excavation unloading effect leads to the phenomenon of stress concentration in the near field of the surrounding

rock, resulting in the formation of the excavation damage zone (EDZ) around the surrounding rock (irreversible plastic deformation), and when the damage develops to a certain extent, the damage zone gradually transitions to the failure zone. The periphery of the damage zone due to the stress concentration zone causes the rock to store high elastic energy but does not exceed its stress intensity, and the paper defines this area as the disturbed zone. Since it is not disturbed, the in-situ stress zone is the deep rock mass at the outer part of the disturbed zone. According to the research results of Jiang et al. based on theoretical calculations and field measurements, it is known that the radius of the failure zone  $R_f = 1.58a$  ( $a$  is the radius of the roadway) and the radius of the damage zone  $R_d = 1.8a$  (Jiang et al. 2007). The junction between the disturbed zone and in-situ stress zone is approximately at the location of  $(3 \sim 5)a$  from the excavation boundary. Figure 4 illustrates the risk zone and stress field distribution laws around the surrounding rock.

The local energy release rate (*LERR*) index is used to assess the magnitude of energy released during the damage of the surrounding rock (Jiang et al. 2010). This index can be calculated using a numerical method, which takes into account the difference between the energy stored in the rock before and after the brittle breakdown. The method ignores the energy release generated by non-brittle breakdown, which does not provide a theoretical value of impact energy. However, this part of energy release is ignored, and the *LERR* index is used to consider the total energy release in the paper. The formula of *LERR* is shown in Eq. (4) (Su et al. 2006).

$$LERR_i = U_{imax} - U_{imin} \quad (4)$$

where  $U_{imax}$  and  $U_{imin}$  are the peak and trough values of elastic strain energy intensity before and after the brittle damage of unit  $i$ , respectively. The formulas are shown in Eqs. (5) and (6).

$$U_{imax} = \frac{[\sigma_1^2 + \sigma_2^2 + \sigma_3^2 - 2\nu(\sigma_1\sigma_2 + \sigma_2\sigma_3 + \sigma_1\sigma_3)]}{2E} \quad (5)$$

$$U_{imin} = \frac{[\sigma_1'^2 + \sigma_2'^2 + \sigma_3'^2 - 2\nu(\sigma_1'\sigma_2' + \sigma_2'\sigma_3' + \sigma_1'\sigma_3')]}{2E} \quad (6)$$

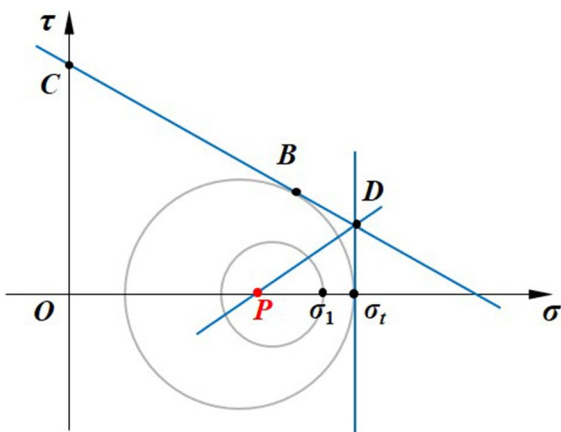


**Fig. 3** Analysis diagram of tensile-shear failure (Zhou et al. 2005)



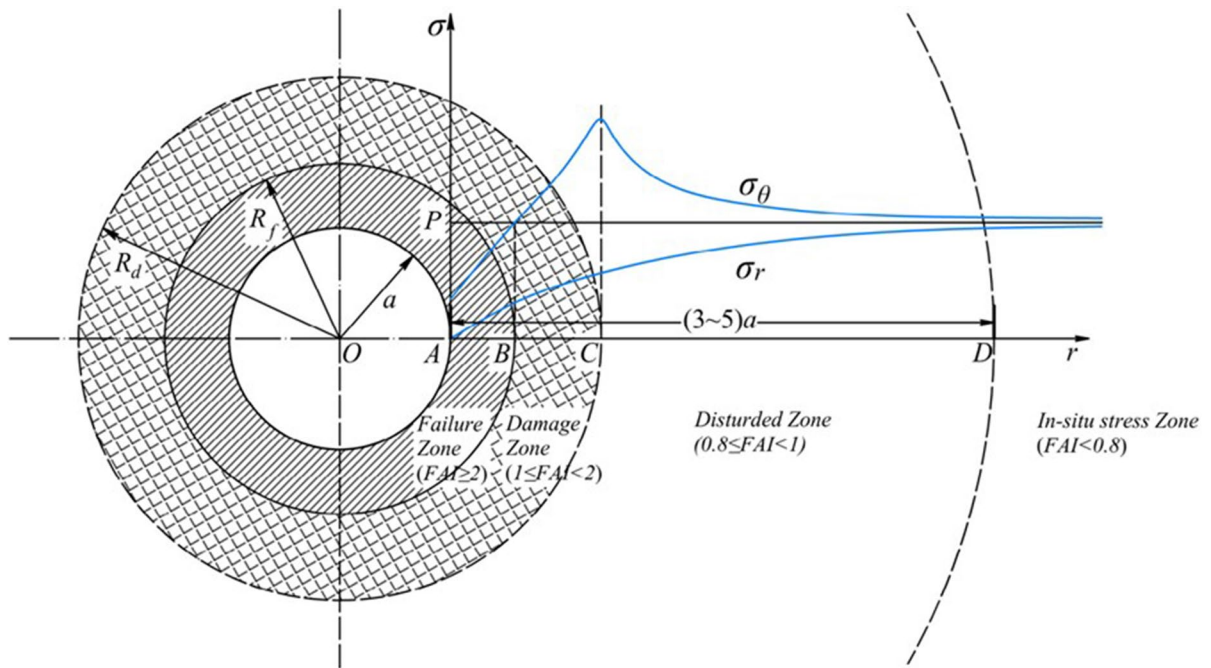


**Fig. 4** Schematic diagram of the risk zone and stress field distribution laws around the surrounding rock

where  $\sigma_1$ ,  $\sigma_2$  and  $\sigma_3$  are the three principal stresses corresponding to peak strain energy of the element and  $\sigma'_1$ ,  $\sigma'_2$  and  $\sigma'_3$  are the three principal stresses corresponding to trough strain energy of the element.  $\nu$  is Poisson’s ratio and  $E$  is Young’s modulus.

### 3 Model Establishment and Parameters Selection

#### 3.1 Model Establishment

To study the mechanical behaviour of the surrounding rock and the distribution and evolution of rockburst risk zones during tunnel excavation with different structural plane shapes, four different working conditions were modelled and analyzed for the tunnel without the structural plane, the tunnel with the exposed inclined structural plane, the tunnel with the unexposed inclined structural plane and the tunnel with the vertical structural plane in the sidewall. To better fit the practical engineering background, a numerical model was established based on the actual engineering dimensions of the site, using the headrace tunnel at the Jinping II hydropower station as a reference. The numerical model size is 60 m × 60 m × 10 m, and

the tunnel form is a straight-walled arch with a size of 13 m × 13 m. The tunnel models for four different structural plane shapes are summarized in Fig. 5.

Considering the damage behaviour of the rock mass under the high-stress field, the geo-stress field at the location of the extremely intense rockburst that had occurred in the headrace tunnel of the Jinping II hydropower station was selected as the boundary condition of the numerical model. The geo-stress measurement is the determination of the undisturbed virginal stress field existing around the mining engineering, which is done by measuring the stress state at certain measurement points in the virginal three-dimensional geo-stress field. The three-dimensional stress state at a point in the rock mass can be represented by six stress components ( $\sigma_x$ ,  $\sigma_y$ ,  $\sigma_z$ ,  $\tau_{xy}$ ,  $\tau_{xz}$ ,  $\tau_{yz}$ ) in the selected coordinate system, as shown in Fig. 6. The magnitude and direction of the three principal stresses at the point can be solved uniquely from the six stress components. The results of in-situ geo-stress measurements show the stress components of a measurement point under the virginal stress field in Table 1. The magnitude and direction of the three principal stresses can be calculated, the maximum principal stress is 62.2 MPa, the intermediate

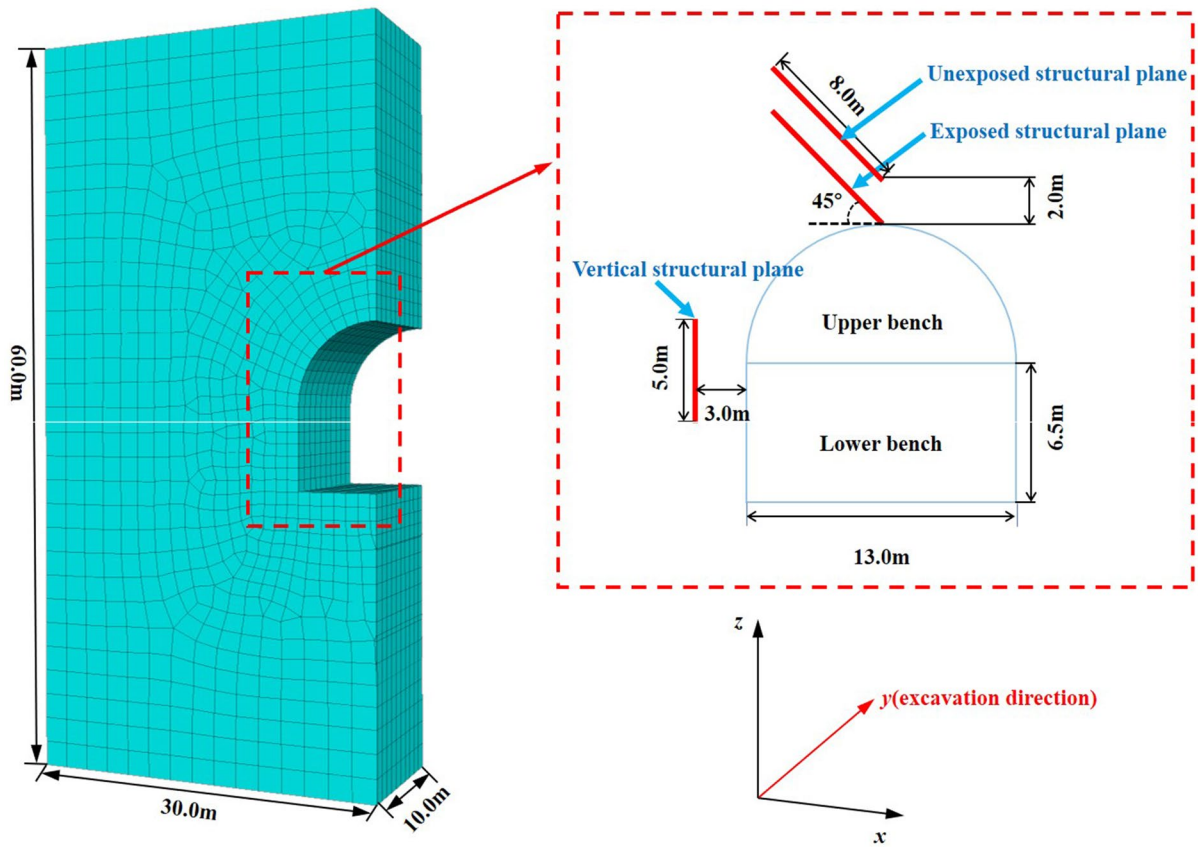


**Fig. 5** Schematic diagram of tunnel excavation models with four different structural plane shapes

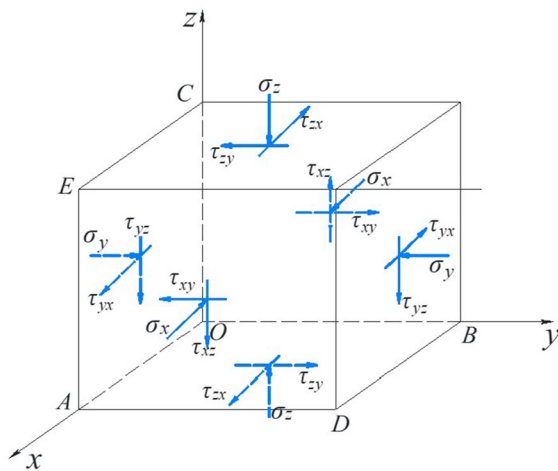


**Fig. 6** Schematic diagram of the geo-stress state at a point in the rock mass

principal stress is 52.6 MPa, and the minimum principal stress is 44.8 MPa. The direction of the maximum principal stress deviates 25° to the left from the central axis of the tunnel excavation surface, the direction of the minimum principal stress is perpendicular to the direction of the maximum principal stress, and the direction of the intermediate principal stress is consistent with the axis of the tunnel (y-axis). The distribution of the geo-stress field is shown in Fig. 7. Note that in  $FLAC^{3D}$ , the stress sign is specified as positive for tension and negative for compression.

The tunnel is excavated by the bench method, which is divided into 10 excavation steps, each with cyclic footage of 1 m, and the excavation process diagram is shown in Fig. 8. In each excavation step, the upper step is excavated first. Then the lower step is excavated until the tunnel runs through. During the numerical simulation, the number of time steps required during each excavation cycle also varies,

**Table 1** Geo-stress components (Zhang et al. 2013)

Components	$\sigma_x$ /MPa	$\sigma_y$ /MPa	$\sigma_z$ /MPa	$\tau_{xy}$ /MPa	$\tau_{yz}$ /MPa	$\tau_{xz}$ /MPa
Value	-46.42	-51.68	-61.48	-2.37	-0.64	3.45

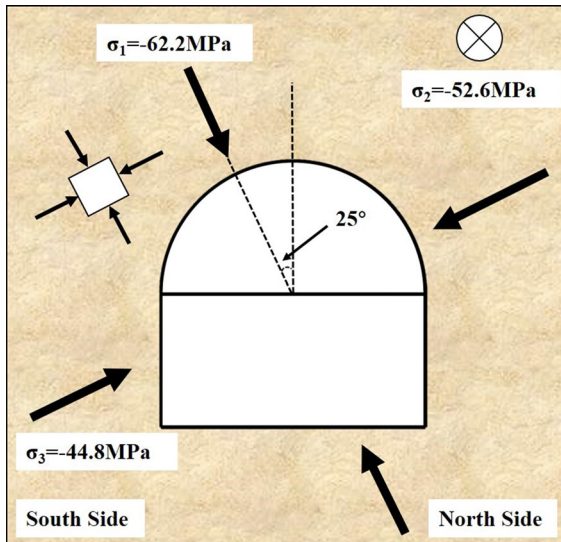


**Fig. 7** Schematic diagram of geo-stress field distribution

where the number of calculation steps required for different 3D geometric models corresponding to the actual engineering excavation process is recorded in detail in Table 2. To study the evolution process of rockburst risk zones in the surrounding rock, a monitoring surface was set up at  $y=0.5$  m. The numerical

simulation results under different excavation progress were compared and analyzed.

### 3.2 Selection of Calculation Parameters

The T2b marble of the Jinping II hydropower station was selected to simulate the deep hard rock tunnelling process, and the detailed rock mechanical parameters are shown in Table 3. The tunnel rock is lithologically consistent with the surrounding rock, giving the same mechanical parameters, in which the plastic shear strain limit for cohesion and the plastic shear strain limit for friction angle are two crucial parameters of the *CWFS* model. Their values can be used as a measure of the critical value when the rock is destroyed. *FLAC<sup>3D</sup>* has a comprehensive range of built-in intrinsic constitutive models in which the strain softening model in the plastic model is applied to simulate the mechanical behaviour of the *CWFS* model. Applying the Table command in the program defines the value of one variable (cohesion, internal friction angle) to vary with the value of another variable (accumulated plastic shear strain). The parameters of the contact plane in *FLAC<sup>3D</sup>* were used to simulate structural planes, and the detailed parameters are shown in Table 4.

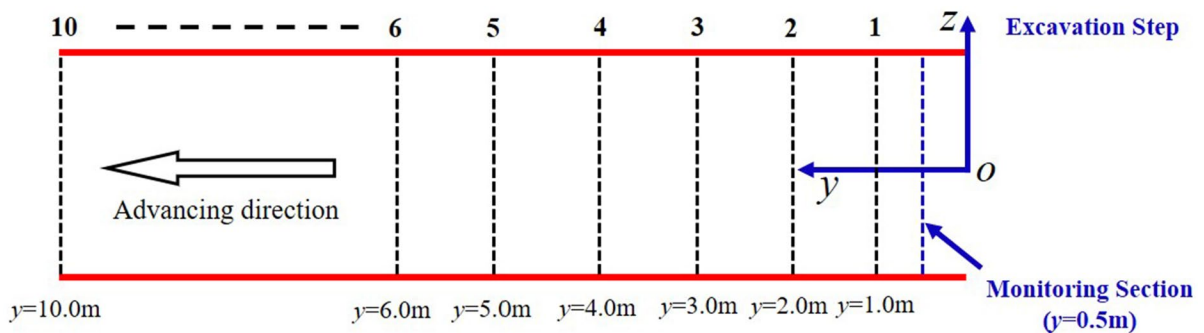


**Fig. 8** Sketch of the excavation of the tunnel in numerical simulation

**Table 2** Numerical simulation calculation steps statistics

Excavation Step	Model A <sup>a</sup>	Model B <sup>b</sup>	Model C <sup>c</sup>	Model D <sup>d</sup>
1(y = 0~1.0 m)	2073	2296	2234	2078
2(y = 1.0~2.0 m)	2088	2085	2087	2081
3(y = 2.0~3.0 m)	2461	2453	2481	2405
4(y = 3.0~4.0 m)	2618	2653	2669	2594
5(y = 4.0~5.0 m)	2791	2799	2855	2735
6(y = 5.0~6.0 m)	2681	2818	2819	2622
7(y = 6.0~7.0 m)	2760	2865	2905	2661
8(y = 7.0~8.0 m)	2819	2979	2998	2744
9(y = 8.0~9.0 m)	2856	3019	3049	2823
10(y = 9.0~10.0 m)	2966	3175	3247	2992
Total steps	26,113	27,142	27,344	25,735

<sup>a</sup>Tunnel without the structural plane<sup>b</sup>Tunnel with the exposed inclined structural plane<sup>c</sup>Tunnel with the unexposed inclined structural plane<sup>d</sup>Tunnel with the vertical structural plane in the sidewall**Table 3** Mechanical parameters for Jinping II T2b marble (Zhang et al. 2013)

Parameters	Value
Elastic modulus/GPa	18.9
Poisson's ratio	0.23
Density/(kg·m <sup>-3</sup> )	2500
Tensile strength/MPa	3
Initial cohesion/MPa	15.6
Residual cohesion/MPa	7.4
Initial internal friction angle/(°)	25.8
Residual internal friction angle/(°)	39.0
Plastic strain limit for cohesion/%	0.45
Plastic strain limit for friction angle/%	0.90
Dilation angle/(°)	10

**Table 4** Structural plane parameters (Wu et al. 2022)

Parameters	Normal stiffness $k_n$ /GPa	Shear stiffness $k_s$ /GPa	Cohe- sive force (MPa)	Internal friction angle/°	Tensile strength (MPa)
Value	2	0.2	0	25	0

## 4 Results and Discussions

### 4.1 Analysis of Stress Transfer and Risk Zone Evolution Process

#### 4.1.1 Numerical Simulation Results of the Tunnel Excavation Without the Structural Plane

As can be seen from the stress field after the first excavation in Fig. 9a, there is an obvious local stress concentration zone at the perimeter of the surrounding rock around the tunnel under the excavation unloading disturbance, making the surrounding rock extremely susceptible to accumulated damage. As shown in Fig. 9b, c and d, with the excavation of the palm face, the stress of the surrounding rock is gradually released. The distribution pattern of the surrounding rock stress field is gradually stabilized. Two obvious half-moon compressive stress concentration zones are formed on both sides of the tunnel, bending from the arch bottom direction toward the vault. In the process of stress transfer caused by excavation disturbance, the surrounding rock around the tunnel progressively accumulates damage. When the degree of damage reaches the limit value, the rock body is destroyed. For hard and brittle rock, it is highly susceptible to inducing rockburst disaster.

As shown in Fig. 10b, the damage occurred firstly around the straight walls on both sides of the tunnel at the end of the fourth excavation, which gradually transitioned from the damage zone formed in the local area after the first excavation to the failure zone. At the same time, the disturbed zone around the tunnel also transitioned to the damage zone. The relationship between the disturbed zone, the damage zone and the failure zone varies dynamically with the excavation process, and the rockburst risk is enhanced accordingly. As shown in Fig. 10b, c and d, with the excavation process, the failure zone on the south side



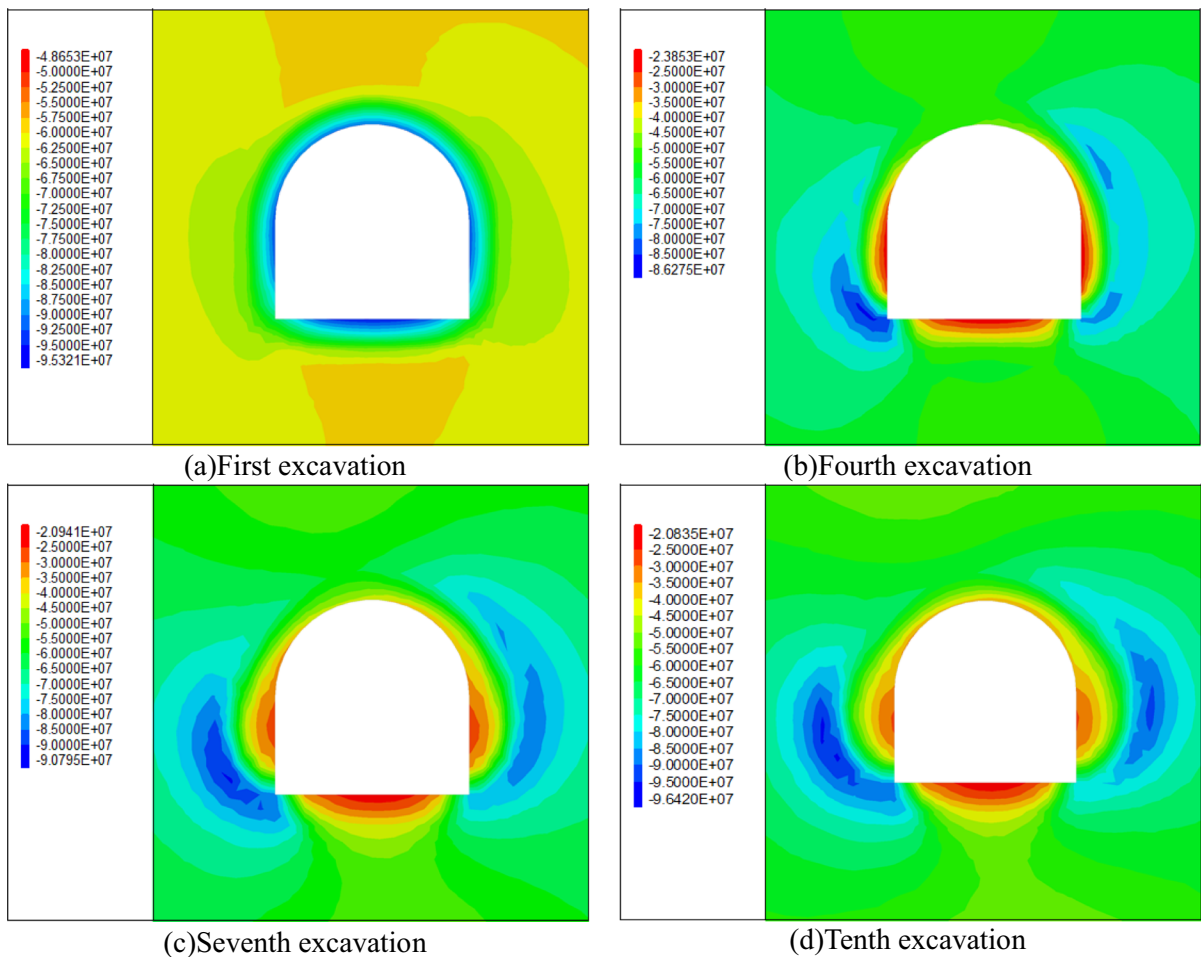


**Fig. 9** Evolution process of maximum principal stress field of the tunnel without the structural plane at monitoring surface(unit:Pa)

of the tunnel is gradually expanding outward, eventually forming a cross-section of a “V”-shaped rockburst risk zone.

As shown in Fig. 11, the simulation results are close to the location of the “7–14” rockburst the headrace tunnel of the Jinping II hydropower station. The failure zone formed at the location of the right arch shoulder coincides with the appearance of cracks at the right spandrel of the headrace tunnel (Yang et al. 2015). From the distribution of risk zones after the tenth excavation in Fig. 10d, the distribution of rockburst risk

zones around the tunnel is approximately perpendicular to the direction of the maximum principal stress component in the geo-stress field.

#### 4.1.2 Analysis of the Mechanism of the Structural Plane Effect

By comparing the results of tunnel excavation with and without the structural plane, while considering the structural plane under different exposure forms, the mechanism of the structural plane effect

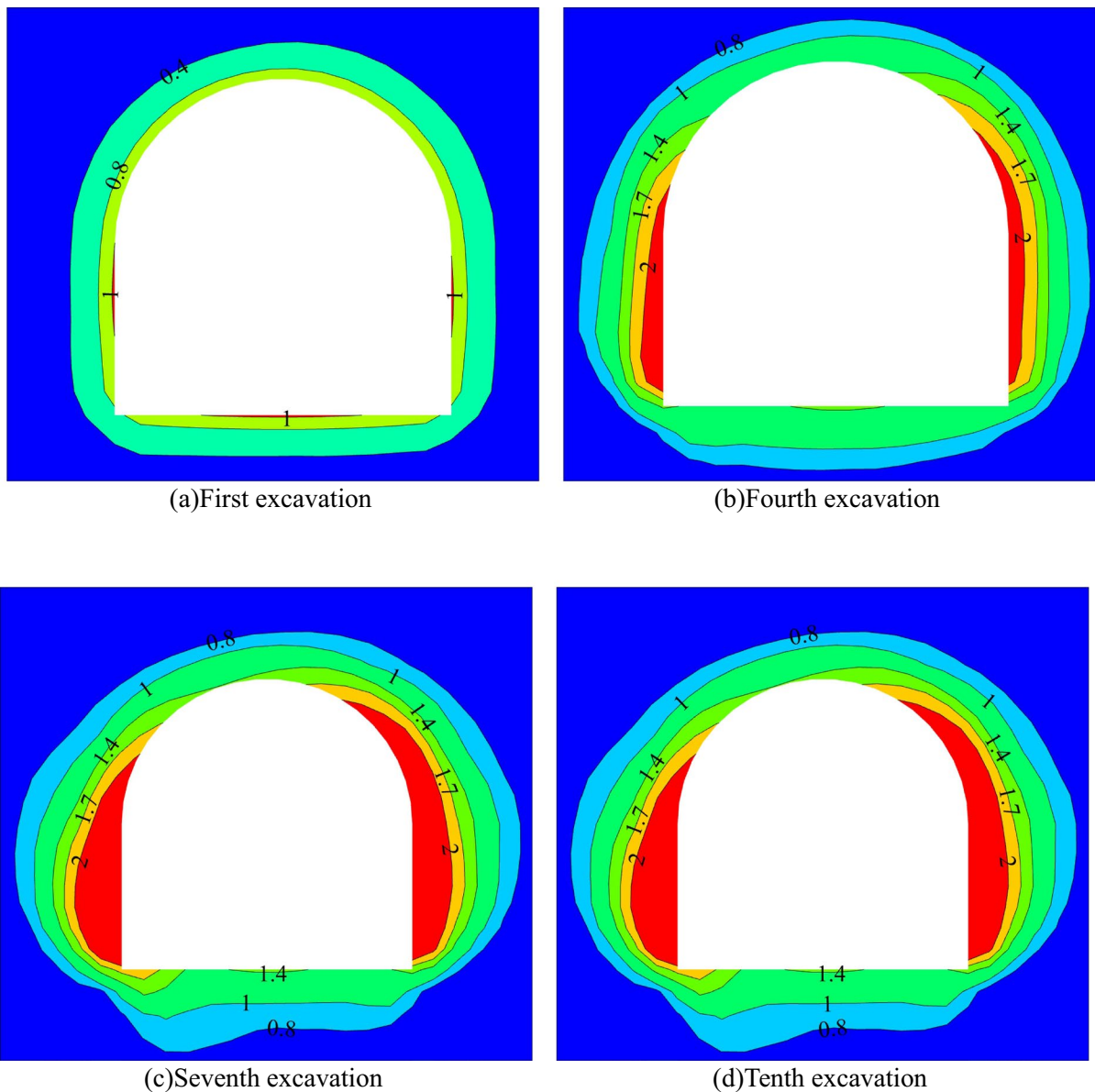


**Fig. 10** Distribution and evolution process of rockburst risk zones of the tunnel without the structural plane at monitoring surface

in the tunnel excavation process is investigated. The exposed structural plane is revealed after the first excavation of the tunnel. In contrast, the unexposed structural plane is always hidden inside the surrounding rock. Hence, the distribution of the stress field in the surrounding rock is different owing to the different working conditions.

In the case of the exposed structural plane, the compressive stress is gathered at the unexposed end

of the structural plane(A'), while the exposed end(A) is in a state of stress release. In contrast to the tunnel without the structural plane, the tunnel with exposed structural planes leads to stress release in a larger area of the rock on the exposed side of the structural plane, as shown in Fig. 12. Figure 12 illustrates the distribution of the maximum principal stress field in the surrounding rock at the monitoring section ( $y=0.5$  m) after the completion of the tenth excavation (after the

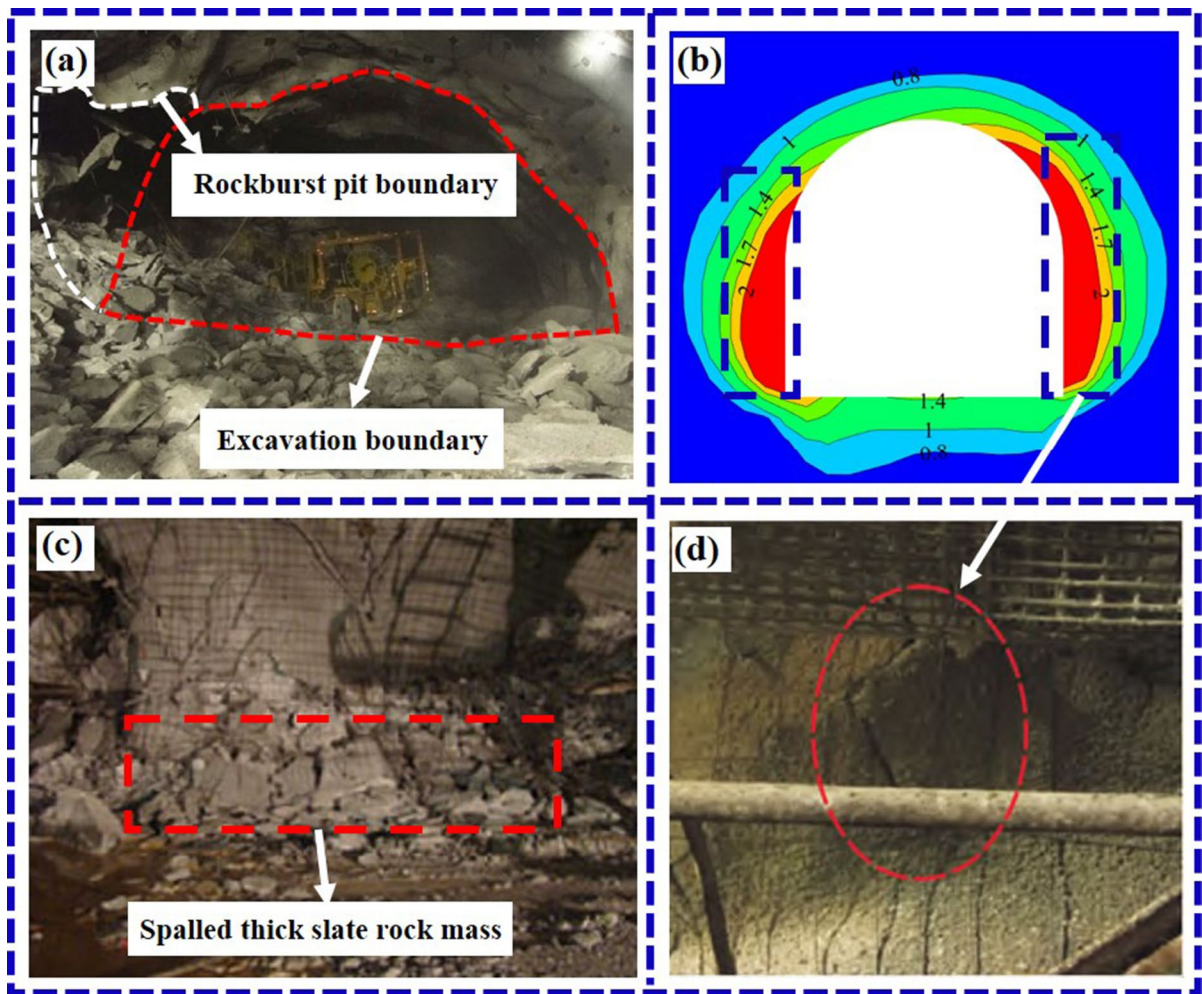


**Fig. 11** Comparison between numerical simulation results and rockburst location at the site. **a** failure of the surrounding rock mass from the left sidewall to the left arch foot. **b** distribution of rockburst risk zones of the tunnel in the numerical

simulation. **c** slabbing of the shotcrete and shallow rock mass at the left arch foot. **d** cracks at the right spandrel of the tunnel. (Zhang et al. 2013; Yang et al. 2015)

tunnel model has been fully through) for the tunnel with the exposed structural plane.

The structural plane endpoint A was selected as the monitoring point to study the evolution of the maximum principal stresses and *FAI* in the surrounding rock. As shown in Fig. 13, the maximum principal stress at point A for the tunnel model with the exposed structural plane decreases from 87.0 to 18.3 MPa, a decrease of 79.0%. The maximum principal stress at point A for the model without the structural plane reduces from 95.1 to 37.4 MPa, a reduction of 60.7%.

Under the combination of the structural plane effect and the excavation unloading effect, the stress in the rock near point A is released sharply, resulting in a rapid release of energy from the surrounding rock. Compared with the tunnel without the structural plane, the *FAI* of the tunnel with the exposed structural plane intensifies and increases and enters the rockburst risk zone after the completion of the third excavation ( $FAI=2.05$ ). The risk of rockburst gradually aggravates with the excavation process. The *FAI* of point A of the tunnel model with the exposed structural plane reaches 2.7 after the completion of excavation (tenth excavation), which is 37.0% higher

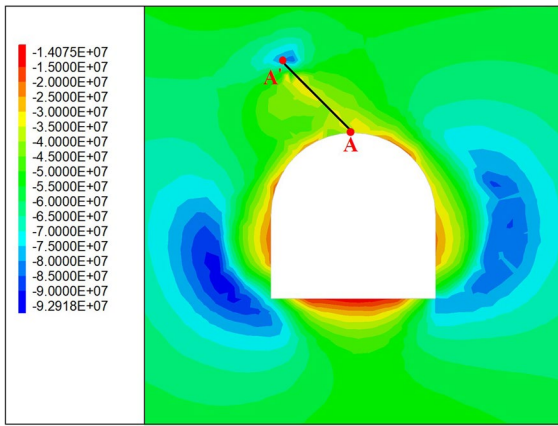


**Fig. 12** Maximum principal stress field distribution diagram of the tunnel with the exposed structural plane after excavation (unit:Pa)

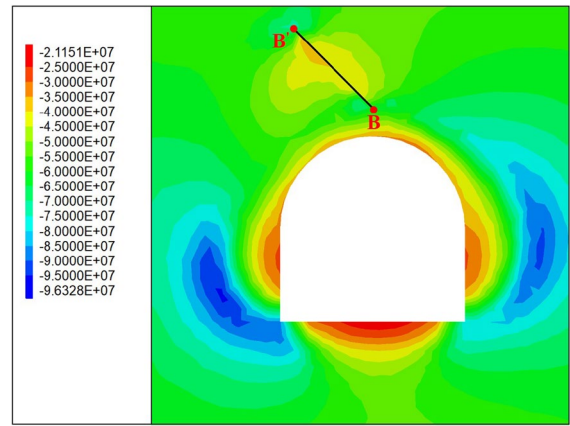


**Fig. 14** Maximum principal stress field distribution diagram of the tunnel with the unexposed structural plane after excavation (unit:Pa)

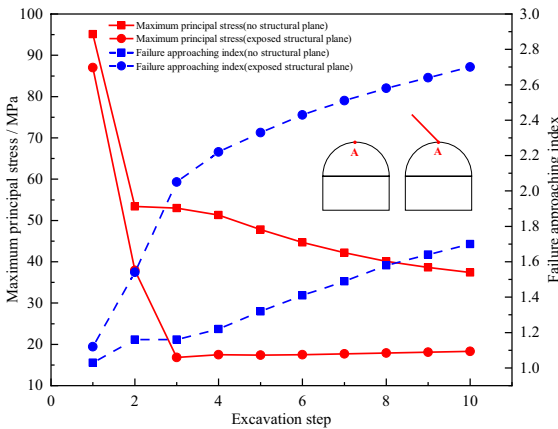


**Fig. 13** Evolution curves of maximum principal stress and FAI at the monitoring point A

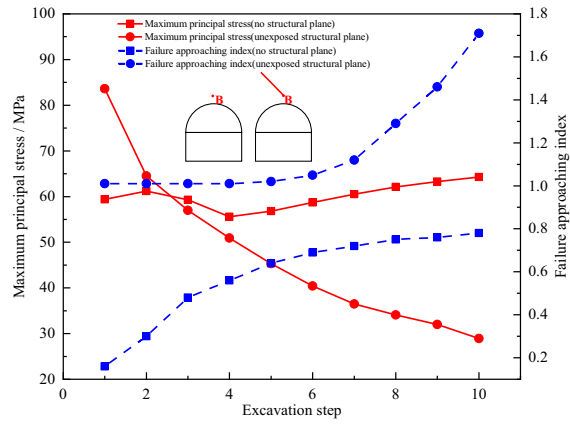


**Fig. 15** Evolution curves of maximum principal stress and FAI at the monitoring point B

than the FAI of point A of the tunnel model without the structural plane (FAI=1.7) after completion of excavation (tenth excavation). The study has shown that the presence of the structural plane is more vulnerable to trigger rockburst hazards.

Figure 14 shows the distribution of the maximum principal stress field in the surrounding rock at the monitoring section (y=0.5 m) after the completion of the tenth excavation for the tunnel with the unexposed structural plane (after the tunnel model was fully through). Compared with the exposed structural plane, both ends of the unexposed structural plane (B and B') are under stress concentration, resulting

in a high-stress state in the rock between the end of the structural plane (B) and the excavation boundary. Point B on the monitoring surface was selected for study and analysis to study the rock damage caused by the stress concentration phenomenon at the end of the unexposed structural plane. As can be seen in Fig. 15, After the completion of the first excavation, the maximum principal stress at point B for the tunnel containing the unexposed structural plane is 83.6 MPa, which is 29.0% greater than the maximum principal stress at point B for the tunnel without the structural plane (59.4 MPa), which indicates the existence of stress concentration at the end of the structural plane. The stress concentration makes the surrounding



rock extremely susceptible to accumulating damage. However, the *FAI* value increased from 1.01 to 1.29 after the first excavation to the eighth excavation, an increase of 27.8%. The rate of damage accumulation is relatively flat with the excavation process. The reason is mainly due to the obstruction effect of the rock body between the structural plane and the excavation boundary, which makes the cracks at the end of the structural plane(B) not easy to expand, and the structural plane effect is not shown. However, with the continuous excavation of the rock mass, when the unloading disturbance gradually spreads to the vicinity of the structural plane, the structural plane effect is gradually activated, and the degree of damage in the rock mass continuously increases. The *FAI* value increases from 1.29 to 1.71 after the eighth excavation to the tenth excavation, an increase of 32.6%. The change in the maximum principal stress at monitoring point B during the tunnel excavation without the structural plane is not obvious, and the influence of the excavation unloading effect is not significant. The *FAI* value of the completed excavation of the tunnel model with the unexposed structural plane is 1.71, which is 54.4% higher than the *FAI* value of the completed tunnel excavation model without the structural plane ( $FAI=0.78$ ). It can be seen that the existence of the structural plane makes the influence of excavation disturbance intensify from the *FAI* evolution curve in Fig. 15. The combination of the excavation disturbance effect and the structural plane effect leads to a dramatic aggravation of the rock mass damage.

#### 4.1.3 Comparative Analysis of Rockburst Risk Zones Induced by the Exposed and Unexposed Structural Plane

In comparing the evolution of rockburst risk zones in tunnels with the exposed and unexposed structural planes in Fig. 16 and 17, there are differences in the effect played by the structural plane under different exposure forms. The differences are summarized as follows:

- (1) The development process of rockburst is accelerated in the tunnel with the exposed structural plane. On the contrary, the formation process of the rockburst risk zones in the tunnel with the unexposed structural plane is relatively slower. The rockburst development process is concealed

and lagged. In contrast to the period of formation of the rockburst risk zones in the vicinity of the structural plane during excavation, the rockburst risk zones are formed at the vault in the tunnel with the exposed structural plane after the third excavation, while the rockburst risk zones are formed in the tunnel with the unexposed structural plane only after the eighth excavation. The conclusion can be visualized in Fig. 18.

- (2) Compared to the tunnelling process containing the exposed structural plane, the unexposed structural plane is not activated at the beginning of tunnel excavation (the structural plane effect is not shown), which is dominated by the excavation unloading effect. However, once the structural plane is activated, the rock body between the tunnel excavation boundary and the structural plane will be rapidly damaged, generating a larger failure zone. This variation can be apparent by comparing the distribution of risk zones after the eighth and tenth excavation of the tunnel with the unexposed structural plane in Fig. 17c and d.

#### 4.1.4 Numerical Simulation Results of the Tunnel Excavation with the Vertical Structural Plane in the Sidewall

Figure 19 illustrates the evolution of the rockburst risk zones at the monitoring surface of the tunnel with the vertical structural plane in the sidewall. As shown in Fig. 19a, the distribution of the risk zone after the first excavation can be seen at the intersection of the southern arch shoulder and the straight wall, the rock mass near the excavation boundary opposite to the structural plane is the first to accumulate damage, and a small area of rock mass near the structural plane also enters the damage zone. The rock near the straight wall area on both sides of the tunnel enters the damage zone under the influence of cumulative excavation disturbance after the completion of the fourth excavation, and the damage zone in the straight wall area on the south side is larger under the influence of vertical structural plane, as shown in Fig. 19b. As shown in Fig. 19b, c and d, with the continuous advancement of the excavation face, the failure zone formed by the rock near the excavation boundary opposite to the structural plane gradually spreads toward the vertical structural plane. The



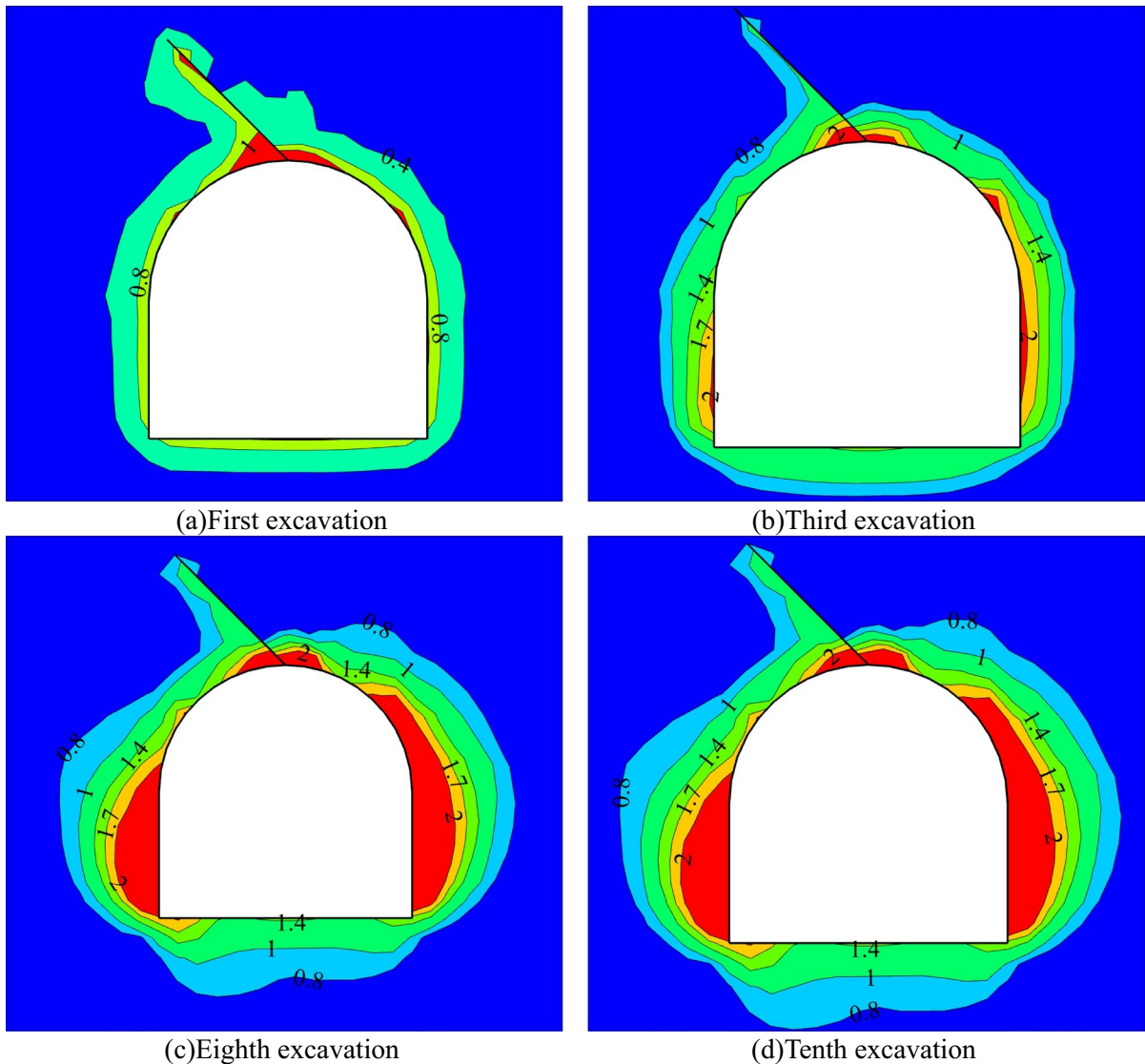


**Fig. 16** Distribution and evolution process of rockburst risk zones of the tunnel with the exposed structural plane at monitoring surface

location of the structural plane becomes the boundary of the failure zone, forming a shape similar to a pan-shaped rockburst risk zone on the south side of the tunnel between the excavation boundary and the structural plane. The simulation result coincides with the situation of the Jinping II hydropower station after the “2–14” extremely intense rockburst described by Zhou et al.(2015a).

#### 4.2 Analysis of Displacement Field Distribution Characteristics

The unloading disturbance effect of the tunnel excavation leads to a rebound tendency of the surrounding rock towards the excavation surface, resulting in corresponding deformation and displacement. As the excavation surface continues to advance, the deformation of the surrounding rock continues to accumulate.

As shown in Fig. 20a, when the tunnel excavation is completed, the surrounding rock displacement

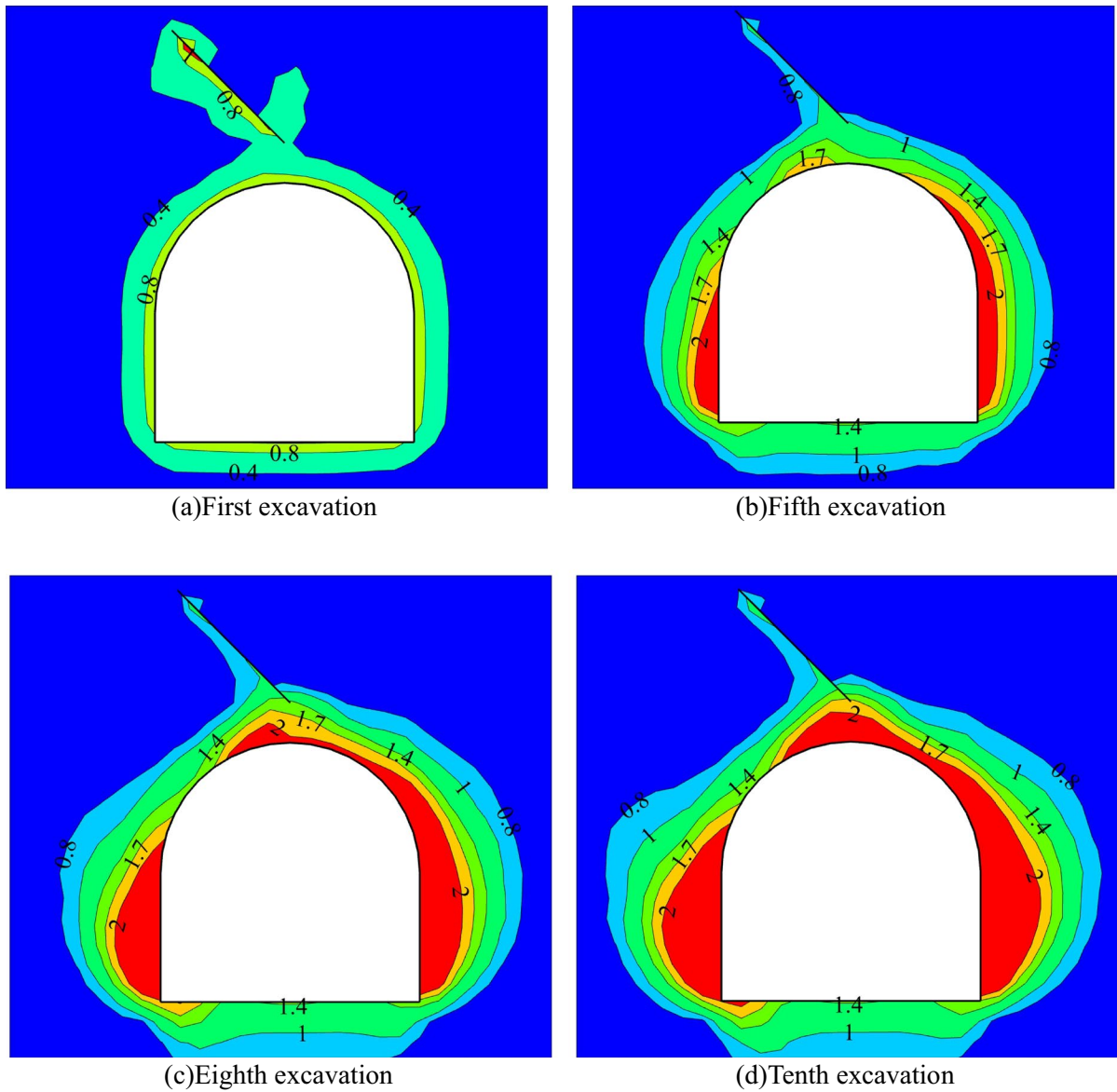


**Fig. 17** Distribution and evolution process of rockburst risk zones of the tunnel with the unexposed structural plane at monitoring surface

values on both sides of the straight wall and the arch bottom are larger, with a maximum displacement of 49.9 mm. The surrounding rock’s displacement field is arch-shaped, and the displacement values were smaller as it moved outward away from the excavation face. Comparison between Fig. 20a and b shows that the distribution of the surrounding rock displacement field is similar on both sides of the straight wall and the arch bottom, and the difference is the distribution

of the surrounding rock displacement field near the structural plane. By comparing the displacement of the surrounding rock on the upper and lower plates of the structural plane in Fig. 20b, the displacement of the surrounding rock on the lower plate of the structural plane is larger compared to the surrounding rock on the upper plate of the structural plane, indicating that the lower plate of the structural plane is moving toward the excavation and generating slip and

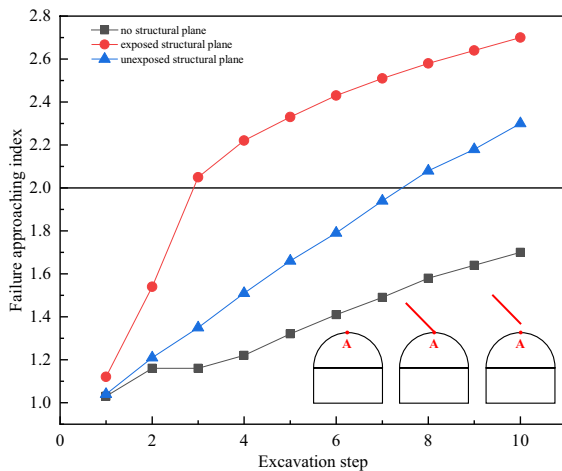


**Fig. 18** Evolution curves of *FAI* at the monitoring point A under different structural plane shapes

dislocation on the structural plane, resulting in larger displacement near the exposed end of the structural plane.

Comparing the distribution of the displacement field of the tunnel with the exposed structural plane (Fig. 20b) and the unexposed structural plane (Fig. 20c), the maximum displacement of the tunnel with the exposed structural plane (51.7 mm) is 1.8 mm greater than the maximum displacement of the tunnel with the unexposed structural plane (49.9 mm). Meanwhile, there are differences in the surrounding rock displacement field distribution. The source of rock mass deformation near the exposed end of the structural plane is the slip and dislocation generated by the structural plane under the influence of excavation disturbance. However, the deformation of the rock between the unexposed structural plane and the excavation boundary originates from the accumulation of deformation under stress concentration caused by the combination of the structural plane effect and the excavation unloading effect. The excessive deformation of the rock mass leads to the rupture of the rock mass, forming a V-shaped area with large displacement values at the tunnel excavation boundary. Therefore, the comparative analysis shows differences in the deformation mechanism of the surrounding rock under different exposure forms of the structural plane.

As shown in Fig. 20d, the rock mass between the left straight wall to the vertical structural plane

generates larger displacement values and has a wider area of larger displacement values than the rock mass near the right straight wall. Meanwhile, comparing Fig. 19a and d, the maximum displacement on the side with the structural plane in Fig. 19d (52.1 mm) is 2.2 mm greater than the maximum displacement on the same side without the structural plane in Fig. 19a (49.9 mm). In conclusion, the existence of the structural plane makes the displacement field of the surrounding rock change, especially in the rock mass near the structural plane. The structural plane effect plays an important role.

#### 4.3 Comparative Analysis of Local Energy Release Rate

The evolution curves of *LERR* at monitoring point A (the vault) under different exposure forms of structural planes is shown in Fig. 21. The *LERR* at monitoring point A after the completion of tunnel excavation without the structural plane is  $79.6 \text{ kJ}\cdot\text{m}^{-3}$ . Comparing the evolution of the *LERR* at monitoring point A for the tunnel with the unexposed structural plane, it appears that the structural plane effect was not shown in the early stage of excavation (during the previous three excavation processes) for the tunnel with the exposed structural plane. However, with the excavation advancing, the structural plane was gradually activated, and the *LERR* was finally stabilized at  $106 \text{ kJ}\cdot\text{m}^{-3}$ . At the same time, comparing the *LERR* at the vault under different exposure forms, the *LERR* of the exposed structural plane has reached  $139 \text{ kJ}\cdot\text{m}^{-3}$  after the first excavation, and it is predictable that the rock in the local area of the vault has a strong proneness to rock burst impact, the *LERR* at point A (tenth excavation) is  $202 \text{ kJ}\cdot\text{m}^{-3}$ , which is  $95.7 \text{ kJ}\cdot\text{m}^{-3}$  greater than the *LERR* at point A (tenth excavation) for the unexposed structural plane, the rockburst strength is stronger compared to the unexposed structural plane.

Combined with the maximum shear force on the structural plane given by the numerical simulation, the maximum shear force on the structural plane of the exposed structural plane (4.8 MPa) is greater than that of the unexposed structural plane (2.6 MPa). Therefore, the presence of intact rock between the excavation boundary and the

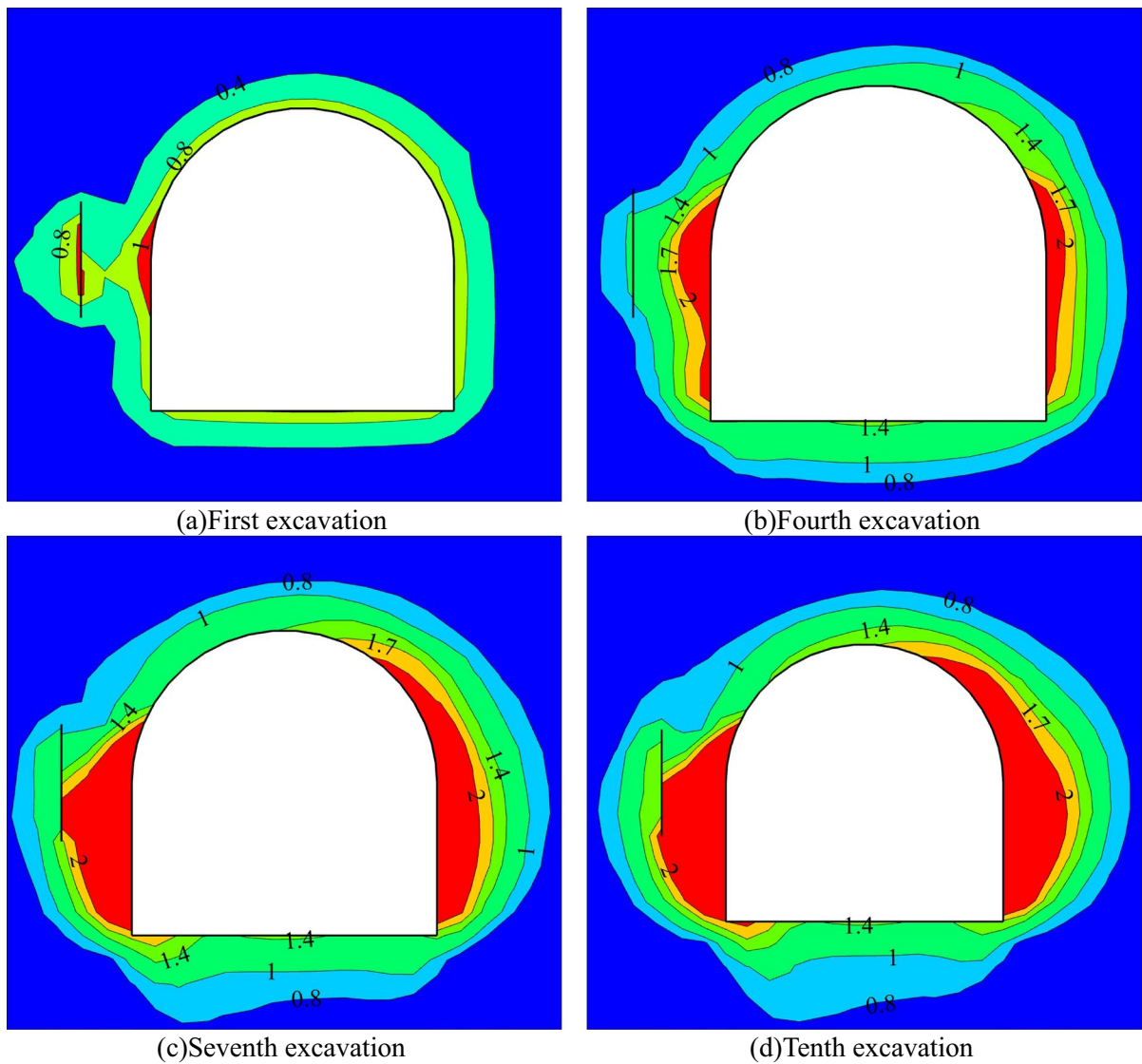


**Fig. 19** Distribution and evolution process of rockburst risk zones of the tunnel with the vertical structural plane in the sidewall at monitoring surface

unexposed structural plane inhibits the activation of the structural plane, making it difficult to activate the structural plane shear and slip mechanisms, and the simulation results are consistent with the conclusions of Feng et al. (2019b).

**5 Conclusion**

Based on numerical analysis indexes and using FLAC<sup>3D</sup> software, taking the Jinping II hydropower

station diversion tunnel as the engineering background, the *CWFS* constitutive model was used for numerical calculation. Modelling and analysis of the tunnelling process under different structural plane shapes to study the surrounding rock’s mechanical behaviour and the distribution and evolution of rockburst risk zones during the excavation process. The main conclusions can be summarized as follows:

- (1) The development process of rockburst in the tunnel with the exposed structural plane is acceler-

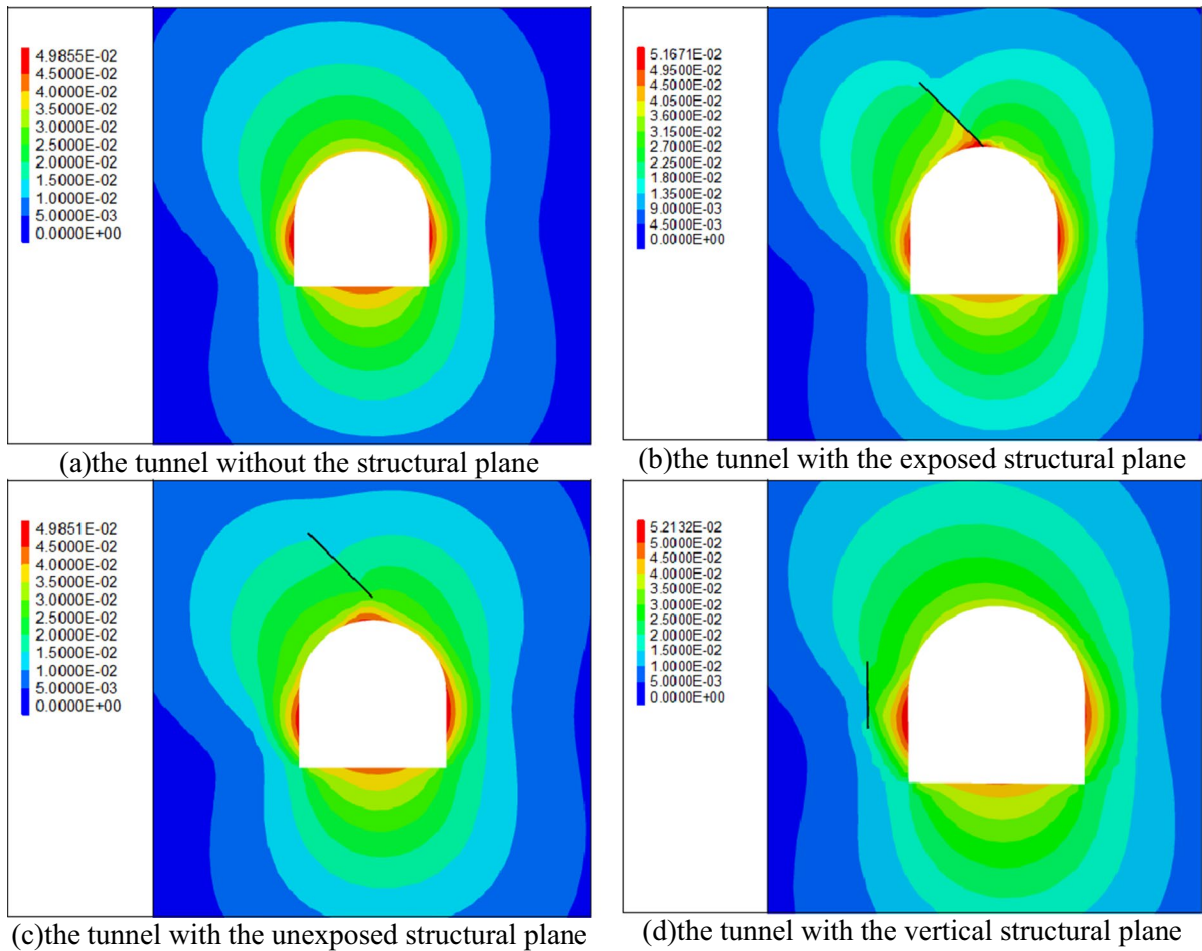


**Fig. 20** Distribution of the surrounding rock displacement field under different structural plane shapes at monitoring surface(unit:m)

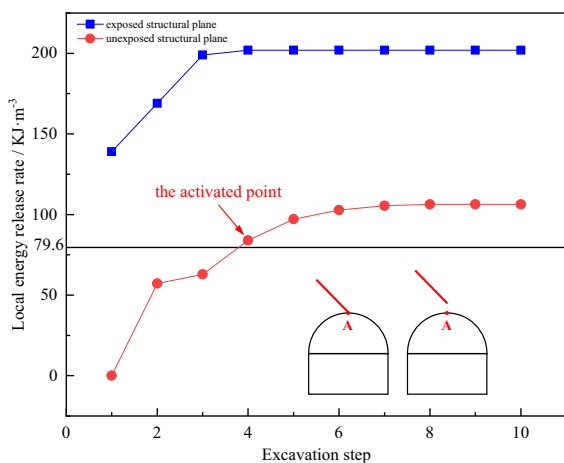


**Fig. 21** Evolution curves of *LERR* at the monitoring point A under different exposure forms of the structural plane

- ated, and the rock around the exposed part of the structural plane has a strong tendency to rockburst impact, and its rockburst strength is higher than that of the tunnel with the unexposed structural plane.
- (2) The development process of rockburst in the tunnel with the unexposed structural plane is slower than in the tunnel with the exposed structural plane. The structural plane effect in the early stage of excavation does not manifest, and the excavation unloading effect mainly dominates. The development process of the rockburst is concealed and lagged. However, once the structural plane is activated, the rock between the structural plane and the excavation boundary is disrupted rapidly, generating a large range of rockburst risk zones.



- (3) In the process of excavation of the tunnel with the vertical structural plane in the sidewall, the location of the structural plane becomes the boundary of the failure zone, forming a shape similar to a pan-shaped rockburst risk zone on the south side of the tunnel between the excavation boundary and the structural plane.
- (4) The existence of the structural plane makes the surrounding rock displacement field to be changed, the structural plane effect plays an important role. There are differences in the deformation mechanism of the tunnel surrounding rock under different exposure forms of the structural plane.

**Author contributions** All authors contributed to the study conception and design. Material preparation, data collection and analysis were performed by Shunchuan Wu, Shun Han, Yongbin Wang, Zhigen Zhu, Long Chen and Yangyang Nian. The first draft of the manuscript was written by Shun Han and all authors commented on previous versions of the manuscript. All authors read and approved the final manuscript.

**Funding** This work was supported by the National Natural Science Foundation of China (Grant No. 51934003), Yunnan Major Scientific and Technological Projects (Grant No. 202202AG050014).

**Data availability** All data generated or analysed during this study are included in this published article.

#### Declarations

**Conflict of interest** The authors have no relevant financial or non-financial interests to disclose.

#### References

- Adoko AC, Gokceoglu C, Wu L et al (2013) Knowledge-based and data-driven fuzzy modeling for rockburst prediction. *Int J Rock Mech Min Sci* 61:86–95. <https://doi.org/10.1016/j.ijrmms.2013.02.010>
- Askari-pour M, Saeidi A, Rouleau A et al (2022) Rockburst in underground excavations: a review of mechanism, classification, and prediction methods. *Underground Space* 7(4):577–607. <https://doi.org/10.1016/j.undsp.2021.11.008>
- Dai L, Pan Y, Li Z et al (2021) Quantitative mechanism of roadway rockbursts in deep extra-thick coal seams: theory and case histories. *Tunn Undergr Space Technol* 111:103861. <https://doi.org/10.1016/j.tust.2021.103861>
- Feng X, Chen B, Ming H et al (2012) Evolution law and mechanism of rockbursts in deep tunnels: immediate rockburst. *Chin J Rock Mech Eng* 31(03):433–444
- Feng X, Xiao Y, Feng G et al (2019a) Study on the development process of rockbursts. *Chin J Rock Mech Eng* 38(04):649–673. <https://doi.org/10.13722/j.cnki.jrme.2019.0103>
- Feng F, Li X, Rostami J et al (2019b) Modeling hard rock failure induced by structural planes around deep circular tunnels. *Eng Fract Mech* 205:152–174. <https://doi.org/10.1016/j.engfracmech.2018.10.010>
- Feng G, Feng X, Chen B et al (2019c) Effects of structural planes on the microseismicity associated with rockburst development processes in deep tunnels of the Jinping-II Hydropower Station, China. *Tunn Undergr Space Technol* 84:273–280. <https://doi.org/10.1016/j.tust.2018.11.008>
- Feng F, Zhao X, Chen S et al (2021) Effect of structural plane position on hard tunnel failure during excavation unloading subjected to high stresses in deep level mines. *J Central S Univ Sci Technol* 52(8):2588–2600. <https://doi.org/10.11817/j.issn.1672-7207.2021.08.007>
- Hajiabdolmajid V, Kaiser P (2003) Brittleness of rock and stability assessment in hard rock tunneling. *Tunn Undergr Space Technol* 18(1):35–48. [https://doi.org/10.1016/S0886-7798\(02\)00100-1](https://doi.org/10.1016/S0886-7798(02)00100-1)
- Huang F, Zhu H, Xu Q et al (2013) The effect of weak inter-layer on the failure pattern of rock mass around tunnel—Scaled model tests and numerical analysis. *Tunn Undergr Space Technol* 35:207–218. <https://doi.org/10.1016/j.tust.2012.06.014>
- Jiang B, Zhang Q, He Y et al (2007) Elastoplastic analysis of cracked surrounding rocks in deep circular openings. *Chin J Rock Mech Eng* 26(05):982–986. <https://doi.org/10.3321/j.issn:1000-6915.2007.05.017>
- Jiang Q, Feng X, Xiang T et al (2010) Rockburst characteristics and numerical simulation based on a new energy index: a case study of a tunnel at 2,500 m depth. *Bull Eng Geol Env* 69(3):381–388. <https://doi.org/10.1007/s10064-010-0275-1>
- Liang W, Zhao G (2022) A review of long-term and short-term rockburst risk evaluations in deep hard rock. *Chin J Rock Mech Eng* 41(01):19–39. <https://doi.org/10.13722/j.cnki.jrme.2021.0165>
- Liu F, Tang C, Ma T et al (2019) Characterizing rockbursts along a structural plane in a tunnel of the Hanjiang-to-Weihe river diversion project by microseismic monitoring. *Rock Mech Rock Eng* 52(6):1835–1856. <https://doi.org/10.1007/s00603-018-1649-0>
- Manouchehrian A, Cai M (2018) Numerical modeling of rockburst near fault zones in deep tunnels. *Tunn Undergr Space Technol* 80:164–180. <https://doi.org/10.1016/j.tust.2018.06.015>
- Meng F, Zhou H, Wang Z et al (2016) Experimental study on the prediction of rockburst hazards induced by dynamic structural plane shearing in deeply buried hard rock tunnels. *Int J Rock Mech Min Sci* 86:210–223. <https://doi.org/10.1016/j.ijrmms.2016.04.013>
- Snelling PE, Godin L, McKinnon SD (2013) The role of geologic structure and stress in triggering remote seismicity in Creighton Mine, Sudbury, Canada. *Int J Rock Mech*

- Min Sci 58:166–179. <https://doi.org/10.1016/j.ijrmms.2012.10.005>
- Su G, Feng X (2005) Parameter identification of constitutive model for hard rock under high in-situ stress condition using particle swarm optimization algorithm. Chin J Rock Mech Eng 24(17):3029–3034
- Su G, Feng X, Jiang Q et al (2006) Study on new index of local energy release rate for stability analysis and optimal design of underground rockmass engineering with high geostress. Chin J Rock Mech Eng 25(12):2453–2460
- Wang J, Apel DB, Pu Y et al (2021a) Numerical modeling for rockbursts: a state-of-the-art review. J Rock Mech Geotech Eng 13(2):457–478. <https://doi.org/10.1016/j.jrmge.2020.09.011>
- Wang J, Chen G, Xiao Y et al (2021b) Effect of structural planes on rockburst distribution: case study of a deep tunnel in Southwest China. Eng Geol 292:106250. <https://doi.org/10.1016/j.enggeo.2021.106250>
- Weng L, Huang L, Taheri A et al (2017) Rockburst characteristics and numerical simulation based on a strain energy density index: a case study of a roadway in Linglong gold mine, China. Tunn Undergr Space Technol 69:223–232. <https://doi.org/10.1016/j.tust.2017.05.011>
- Wu J, Zhang X, Yu L et al (2022) Rockburst mechanism of rock mass with structural planes in underground chamber excavation. Eng Fail Anal 139:106501. <https://doi.org/10.1016/j.engfailanal.2022.106501>
- Xue R, Liang Z, Xu N (2021) Rockburst prediction and analysis of activity characteristics within surrounding rock based on microseismic monitoring and numerical simulation. Int J Rock Mech Min Sci 142:104750. <https://doi.org/10.1016/j.ijrmms.2021.104750>
- Yang F, Zhou H, Lu J (2015) An energy criterion in process of rockburst. Chin J Rock Mech Eng 34(S1):2706–2714. <https://doi.org/10.13722/j.cnki.jrme.2013.1862>
- Zhang C, Zhou H, Feng X (2007) Stability assessment of rockmass engineering based on failure approach index. Rock Soil Mech 28(5):888–894. <https://doi.org/10.16285/j.rsm.2007.05.008>
- Zhang C, Zhou H, Feng X (2011) An index for estimating the stability of brittle surrounding rock mass: *FAI* and its engineering application. Rock Mech Rock Eng 44(4):401–414. <https://doi.org/10.1007/s00603-011-0150-9>
- Zhang C, Feng X, Zhou H et al (2012) Case histories of four extremely intense rockbursts in deep tunnels. Rock Mech Rock Eng 45(3):275–288. <https://doi.org/10.1007/s00603-011-0218-6>
- Zhang C, Feng X, Zhou H et al (2013) Rockmass damage development following two extremely intense rockbursts in deep tunnels at Jinping II hydropower station, Southwestern China. Bull Eng Geol Env 72(2):237–247. <https://doi.org/10.1007/s10064-013-0470-y>
- Zhang C, Lu J, Chen J et al (2017) Discussion on rock burst proneness indexes and their relation. Rock Soil Mech 38(5):1397–1404. <https://doi.org/10.16285/j.rsm.2017.05.022>
- Zhang C, Li D, Wu S et al (2021) Study on evolution mechanism of structure-type rockburst: insights from discrete element modeling. Sustainability 13(14):8036. <https://doi.org/10.3390/su13148036>
- Zhou H, Zhang C, Feng X et al (2005) Analysis of rock mass stability in tunnel and underground engineering based on yield approach index. Chin J Rock Mech Eng 24(17):3083–3087
- Zhou H, Meng F, Zhang C et al (2015a) Effect of structural plane on rockburst in deep hard rock tunnels. Chin J Rock Mech Eng 34(04):720–727. <https://doi.org/10.13722/j.cnki.jrme.2015.04.008>
- Zhou H, Meng F, Zhang C et al (2015b) Analysis of rockburst mechanisms induced by structural planes in deep tunnels. Bull Eng Geol Env 74(4):1435–1451. <https://doi.org/10.1007/s10064-014-0696-3>
- Zhou J, Li X, Mitri HS (2016) Classification of rockburst in underground projects: comparison of ten supervised learning methods. J Comput Civ Eng 30(5):04016003. [https://doi.org/10.1061/\(ASCE\)CP.1943-5487.0000553](https://doi.org/10.1061/(ASCE)CP.1943-5487.0000553)
- Zhou J, Li X, Mitri HS (2018) Evaluation method of rockburst: state-of-the-art literature review. Tunn Undergr Space Technol 81:632–659. <https://doi.org/10.1016/j.tust.2018.08.029>
- Zhu B, Fan J, Shi X et al (2022) Study on rockburst proneness of deep tunnel under different geo-stress conditions based on DEM. Geotech Geol Eng 40(3):1373–1386. <https://doi.org/10.1007/s10706-021-01969-8>

**Publisher's Note** Springer Nature remains neutral with regard to jurisdictional claims in published maps and institutional affiliations.

Springer Nature or its licensor (e.g. a society or other partner) holds exclusive rights to this article under a publishing agreement with the author(s) or other rightsholder(s); author self-archiving of the accepted manuscript version of this article is solely governed by the terms of such publishing agreement and applicable law.